A Satellite Study of the Relationship between Sea Surface Temperature and Column Water Vapor over Tropical and Subtropical Oceans

KAYA KANEMARU

Graduate School of Environmental Studies, Nagoya University, Nagoya, Japan

HIROHIKO MASUNAGA

Hydrospheric Atmospheric Research Center, Nagoya University, Nagoya, Japan

ABSTRACT

The known characteristics of the relationship between sea surface temperature (SST) and column water vapor (CWV) are reevaluated with recent satellite observations over tropical and subtropical oceans. Satellite data acquired by the *Aqua* Advanced Microwave Scanning Radiometer for Earth Observing System (AMSR-E), Atmospheric Infrared Sounder (AIRS)/Advanced Microwave Sounder Unit (AMSU) suite, the Tropical Rainfall Measuring Mission (TRMM) precipitation radar (PR), and the Quick Scatterometer (QuikSCAT) SeaWinds are analyzed together for 7 years from October 2002 to September 2009. CWV is decomposed into surface humidity, presumably coupled closely to SST, and the water vapor scale height as an index of vertical moisture gradient between the boundary layer and the free troposphere. Surface relative humidity is climatologically homogeneous across tropical and subtropical oceans, while the dependence of CWV on SST varies from one region to another. SST mainly accounts for the variation of CWV with the water vapor scale height, which is virtually invariant over subtropical oceans. On the other hand, over tropical oceans, the variability of CWV is explained not only by SST but also by a systematic change of the water vapor scale height. The regional contrast between tropical and subtropical oceans is discussed in the context of the regional moisture budget including vertical moisture transport through convection.

1. Introduction

Atmospheric water vapor has an important role in maintaining the hydrological cycle on the earth's climate system. Water vapor integrated from the surface to the top of the atmosphere, often called column water vapor (CWV), is known to be related closely with sea surface temperature (SST) over the global ocean (e.g., Prabhakara et al. 1979; Raval and Ramanathan 1989; Stephens 1990; Gaffen et al. 1992; Jackson and Stephens 1995; Wentz and Schabel 2000; Trenberth et al. 2005). Prabhakara et al. (1979) and Stephens (1990) pointed out that the relationship between SST and CWV resembles the Clausius–Clapeyron (C–C) relation. Two major assumptions, however, are required to physically ascribe the SST–CWV

relation to the C–C relation. First, surface relative humidity should be regionally homogeneous so that surface moisture depends exclusively on SST. Second, water vapor at all heights should vary coherently, that is, vertical moisture gradient should be invariable.

The first assumption of the constant surface relative humidity is indeed supported by past observations (Peixoto and Oort 1996; Dai 2006). The second assumption of invariant vertical moisture gradient may be valid regionally (Reitan 1963; Bolsenga 1965), whereas it is less likely the case on a global scale because vertical moisture gradient changes with latitudes and seasons (Smith 1966; Liu and Niiler 1984). The characteristics of the SST–CWV relation indeed differ regionally between tropical and subtropical oceans. Stephens (1990) and Gaffen et al. (1992) found that the SST–CWV relation is not entirely consistent with the C–C relation over tropical oceans. Jackson and Stephens (1995) showed that observed CWV is poorly predicted by the C–C relation with SST over tropical oceans, although the C–C relation is a

Corresponding author address: Kaya Kanemaru, Graduate School of Environmental Studies, Nagoya University, Furo-cho, Chikusa-ku, Nagoya 464-8601, Japan.
E-mail: kanemaru@satellite.hyarc.nagoya-u.ac.jp

reasonable approximation over subtropical oceans. These studies suggest that the assumption of invariant vertical moisture gradient may not hold over tropical oceans.

The regional variability of vertical moisture gradient may be considered to be related to convective activities. Chaboureau et al. (1998) found that the mid- and upper-tropospheric moisture systematically relates with high cloud occurrence by satellite data. Bretherton et al. (2004) and Holloway and Neelin (2009) showed from observational data that the precipitation intensity relates with the free tropospheric (FT) moisture rather than the boundary layer (BL) moisture.

To comprehensively understand the roles of SST and tropospheric moisture in convective development, the systematic regional variation of vertical moisture gradient is investigated in this paper. Recent technological progress in satellite remote sensing has made it possible to observe surface relative humidity and vertical moisture gradient thoroughly across the globe. The purposes of this study are to 1) understand the regional difference in the SST–CWV relation focusing on the potential roles of surface relative humidity and vertical moisture gradient, and 2) discuss the relevance between the regional characteristics of the SST–CWV relation and dynamical environments. Data analyzed are introduced in section 2. Analysis procedures are described in section 3. The results are presented in section 4 and discussed in section 5. Current findings are concluded in section 6.

2. Data

This study uses satellite data from the *Aqua* Advanced Microwave Scanning Radiometer for Earth Observing System (AMSR-E), the *Aqua* Atmospheric Infrared Sounder (AIRS)/Advanced Microwave Sounder Unit (AMSU) suite, the Quick Scatterometer (QuikSCAT) SeaWinds, and the Tropical Rainfall Measuring Mission (TRMM) precipitation radar (PR). The AMSR-E and QuickSCAT products (versions 7 and 4, respectively) are provided by Remote Sensing Systems (RSS). RSS provides daily gridded data with ascending and descending orbits separately stored at $0.25° \times 0.25°$ spatial resolution. The AMSR-E product contains SST and CWV over ocean. The root-mean-square (RMS) error of AMSR-E SST and CWV is $0.58°$C and 0.57 kg m^{-2}, respectively (Wentz and Meissner 2000). The QuikSCAT product contains wind vector and convergence at ocean surface. The RMS difference of QuikSCAT wind speed and direction is 1 m s^{-1} and $23°$, respectively (Ebuchi et al. 2002). Since the accuracy of the wind vector is affected by rain, wind data in raining scenes are excluded using rain flags. This study uses the Level-2 AIRX product version 5 utilizing AIRS and AMSU instruments (hereafter AIRS

collectively) provided by the National Aeronautics and Space Administration (NASA). The AIRS product yields temperature and humidity profiles at about 1-km vertical resolution and 45-km spatial resolution at nadir, where the contamination of clouds is algorithmically cleared (Susskind et al. 2003, 2011). The accuracy of AIRS temperature and humidity estimates is 1 K km^{-1} and 20% (2 km)$^{-1}$, respectively (Tobin et al. 2006), and retains acceptable quality up to 70% of cloud fraction (Fetzer et al. 2006). In this study, AIRS temperature and humidity profiles are analyzed only where flagged as best. The TRMM PR data are provided by the Japan Aerospace Exploration Agency (JAXA) Earth Observation Research Center (EORC). The PR product contains rain profiles at the 250-m vertical resolution and about 5-km horizontal resolution after August 2001 when the TRMM orbit was boosted. Surface rain and vertical rain profiles, averaged to the 1-km vertical resolution, are adopted from the PR 2A25 product version 6 (Iguchi et al. 2000).

All the satellite datasets are projected onto a common $1° \times 1°$ gridded daily data with ascending and descending orbits combined. These data are analyzed for 7 years from October 2002 to September 2009 over all oceans within the latitudinal band between $25°$N and $25°$S. Data are sampled only where both AMSR-E and AIRS observations are available for the analysis in section 4, and where all AMSR-E, AIRS, QuikSCAT, and PR measurements are available for the discussion in section 5. AMSR-E and QuikSCAT data are averaged from the original $0.25° \times 0.25°$ grid to a $1° \times 1°$ grid. AIRS and PR data are averaged from individual footprints in level-2 data to a $1° \times 1°$ grid. AMSR-E, AIRS, and QuikSCAT estimates are interpolated from the neighboring eight grid boxes averaged to fill in pixels contaminated by rain and clouds. The accuracy of interpolated data and the sampling errors caused by missing data are evaluated in appendix B.

3. Analysis procedure

The analysis procedure is introduced in this section. The water vapor scale height H_v is introduced to describe vertical moisture gradient, where

$$H_v \equiv \frac{W}{\rho_{v,s}} = \frac{W}{\rho_a q_{v,s}}. \tag{1}$$

Here, W, $\rho_{v,s}$, ρ_a, and $q_{v,s}$ are CWV, surface water vapor density, the density of dry air (=1.2 kg m^{-3}), and surface water vapor mixing ratio, respectively. Here, H_v is derived from CWV observed by AMSR-E, and $q_{v,s}$ is estimated by AIRS and AMSR-E. The method to estimate
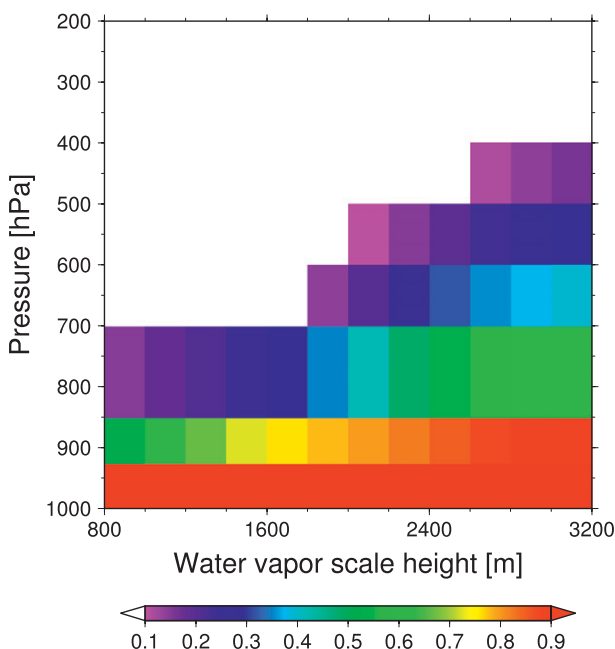
FIG. 1. Vertical profiles of water vapor mixing ratio normalized by its surface value sorted by the water vapor scale height. The normalization is applied to instantaneous measurements before averaged into each scale height bin.

$q_{v,s}$ is described in appendix A. If water vapor density exponentially decreases with height, H_v provides the e-folding scale. Figure 1 shows the scaled vertical structure of moisture sorted as a function of H_v, where water vapor mixing ratio q_v is normalized by its surface value $q_{v,s}$. Figure 1 illustrates that H_v well represents the contrast between the BL and FT water vapor mixing ratios. In this work, H_v is used as a measure quantifying vertical moisture gradient.

A simple analytic equation is derived next as guidance to examine the observed SST–CWV relation. The equation of state for vapor is expressed as

$$\rho_{v,s} = \rho_a q_{v,s} = \frac{e_0}{R_v T_0} = \frac{\mathrm{RH}_0 \times e_s(T_0)}{R_v T_0}, \qquad (2)$$

where $e_0, R_v, T_0, \mathrm{RH}_0$, and $e_s(T_0)$ are surface vapor pressure, the gas constant for water vapor ($=461.5$ J K^{-1} kg^{-1}), surface air temperature, surface relative humidity, and saturation vapor pressure for temperature T_0, respectively; RH_0 is obtained from $q_{v,s}$ and AIRS surface air temperature. Saturated vapor pressure may be written as (Bolton 1980)

$$e_s(T_0) = 6.11 \exp\left(\frac{17.67t}{t + 243.5}\right), \qquad (3)$$

where t is Celsius temperature ($t = T_0 - 273.15$). We rewrite SST and CWV with T_s and W, and substituting

T_s for T_0 to derive the SST–CWV relation, (1) and (2) give

$$\mathrm{RH}_0 \times H_v = \frac{R_v W T_s}{e_s(T_s)}. \qquad (4)$$

Equation (4) shows that $\mathrm{RH}_0 \times H_v$ is a function of SST and CWV. The theoretical relation between SST and $\rho_{v,s}$ is thus written as

$$\mathrm{RH}_0 = \frac{R_v \rho_{v,s} T_s}{e_s(T_s)}. \qquad (5)$$

Equations (4) and (5) are compared with observational results in the next section. In these equations, T_0 has been substituted by T_s for practical convenience, which slightly affects the RH_0 variability to evaluate the relationship between SST and moisture.

4. Results

This section reveals the regional characteristics of the SST–CWV relation over tropical and subtropical oceans. Figure 2a shows the joint probability density function of SST and CWV (solid) with the histogram ridge indicated by thick line over the latitudinal band between 25°N and 25°S. Theoretical lines of $\mathrm{RH}_0 \times H_v$ (dashed) predicted from (4) are also shown. The histogram pattern represents the daily average and overall captures the climatological SST–CWV relation seen in the monthly average (Gaffen et al. 1992; Zhang and Qiu 2008). The histogram ridge follows a theoretical $\mathrm{RH}_0 \times H_v$ line of 1000 m for SSTs lower than 24°C and begins to depart from 1000 to 1500 m for SSTs from 24° to 27°C. The joint histogram of SST and $\rho_{v,s}$ (Fig. 2b) has a ridge in the close vicinity of a RH_0 of 70%–80%. It is implied that RH_0 does not change much over a broad range of SST, as also found by past observations (Peixoto and Oort 1996; Dai 2006). Figure 2 implies that H_v, under a virtually constant RH_0, is also almost invariant for low SSTs. When SST reaches 27°C, the histogram ridge (Fig. 2a) rapidly rises nearly vertically from 1500 to 2000 m while RH_0 remains near 70%–80% (Fig. 2b). Once the ridge reaches near a $\mathrm{RH}_0 \times H_v$ of 2000 m, the histogram ridge ceases to rise. This is confirmed by Fig. 3. Figure 3a offers evidence that the histogram peak extends over a narrow band where observed RH_0 is 80% as seen in Fig. 2b. Observed RH_0 is somewhat higher than inferred from the theoretical line in Fig. 2b, which is because we have replaced T_0 with T_s in (5). Figure 3b shows that H_v stays around 1500 m for relatively low SSTs, while it drastically increases from 1500 to 2500 m for higher SSTs. This result suggests that two distinct regimes
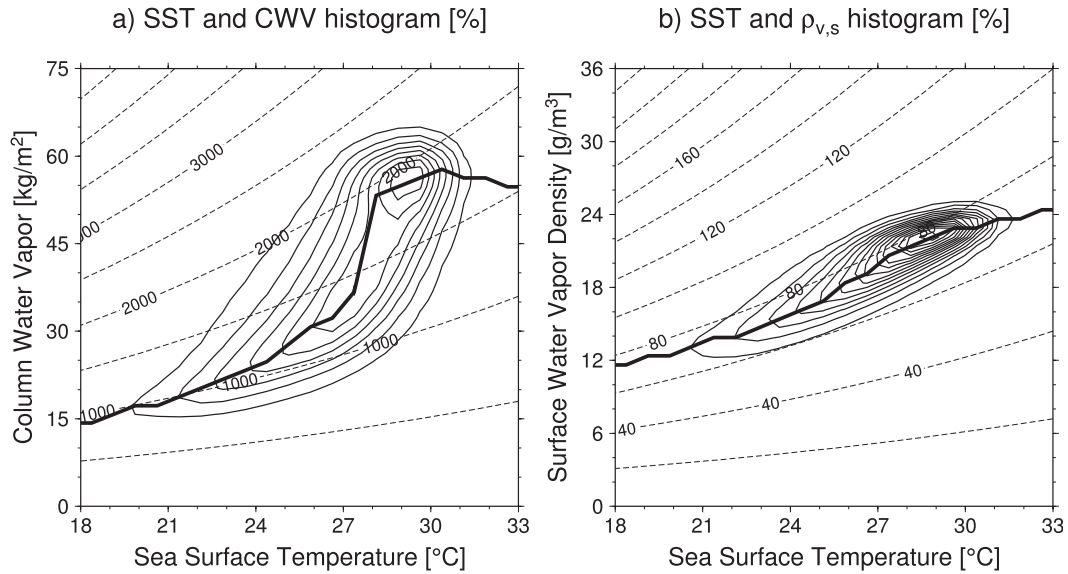
a) SST and CWV histogram [%]   b) SST and $\rho_{v,s}$ histogram [%]

FIG. 2. (a) The joint probability density function (solid lines) of SST and CWV and $RH_0 \times H_v$ predicted from (4) (m; dashed lines). Bin sizes are 0.75°C and 1.5 kg m^{-2}. Contour interval is 0.1%. The thick line shows the maximum occurrence for each SST. (b) As in (a), but for SST and $\rho_{v,s}$ and RH_0 predicted from (5) (%). Bin sizes are 0.75°C and 0.75 kg m^{-3}. Contour interval is 0.2%.

exist with respect to how H_v changes with SST and CWV. In the first regime, CWV is controlled by SST through the C–C relation. On the other hand, CWV is attributed not only to a regional gradient of SST but also to a systematic change in H_v in the second regime. These regimes are separated by SST with a boundary near

27°C. Standard deviations of RH_0 and H_v in the SST–CWV plane are shown in Fig. 4. The climatological means of RH_0 and H_v are well representative of their daily values since standard deviations are both small in the vicinity of the histogram and on its lower right side. The standard deviation is, however, relatively large

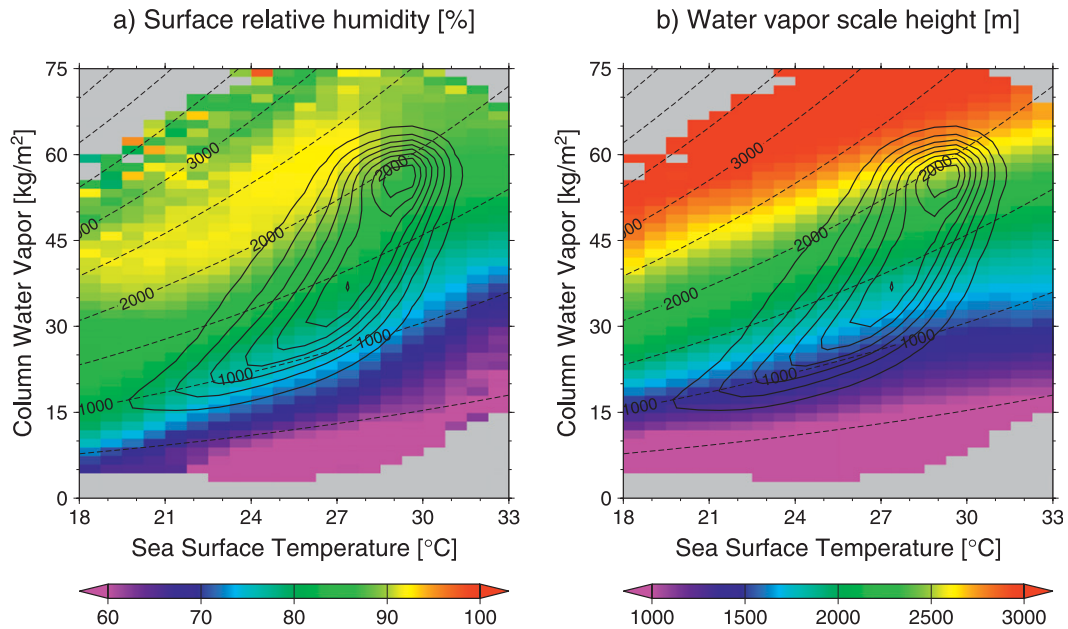a) Surface relative humidity [%]   b) Water vapor scale height [m]

FIG. 3. (a) Surface relative humidity (%) as a function of SST and CWV. (b) As in (a), but for the water vapor scale height (m). Contours and dashed lines are taken from Fig. 2a.

a) Standard deviation of RH_0 [%]
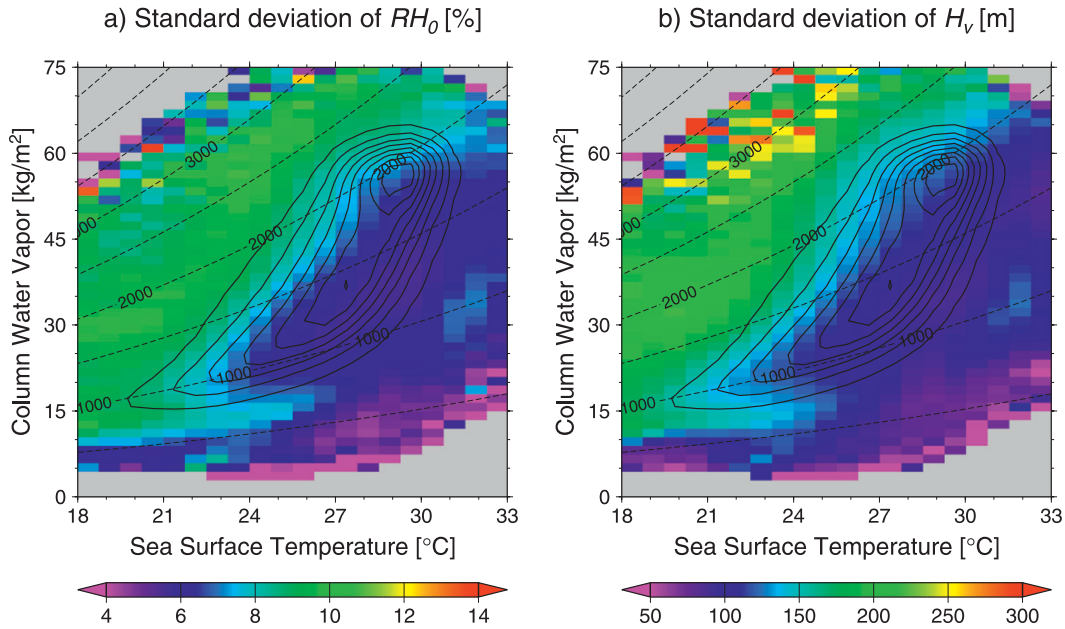
b) Standard deviation of H_v [m]

FIG. 4. As in Fig. 3, but for standard deviation.

where SST is low and CWV is large, which is discussed later.

The findings above are quantitatively assessed next. CWV exhibits contrasting sensitivities to SST depending on SSTs (Fig. 5a) as expected from the results above. The CWV sensitivity to SST is decomposed into different contributions as follows. Differentiating (4) with respect to SST, one finds

$$\frac{\partial \ln W}{\partial T_s} = \frac{\partial \ln RH_0}{\partial T_s} + \frac{\partial \ln H_v}{\partial T_s} + \frac{\partial \ln e_s}{\partial T_s} - \frac{\partial \ln T_s}{\partial T_s}$$
$$= \frac{\partial \ln RH_0}{\partial T_s} + \frac{\partial \ln H_v}{\partial T_s} + \frac{L_v - R_v T_s}{R_v T_s^2}. \qquad (6)$$

Here, L_v is the specific latent heat of vapor ($=2.5 \times 10^6$ J K^{-1} kg^{-1}). The first and second terms on the

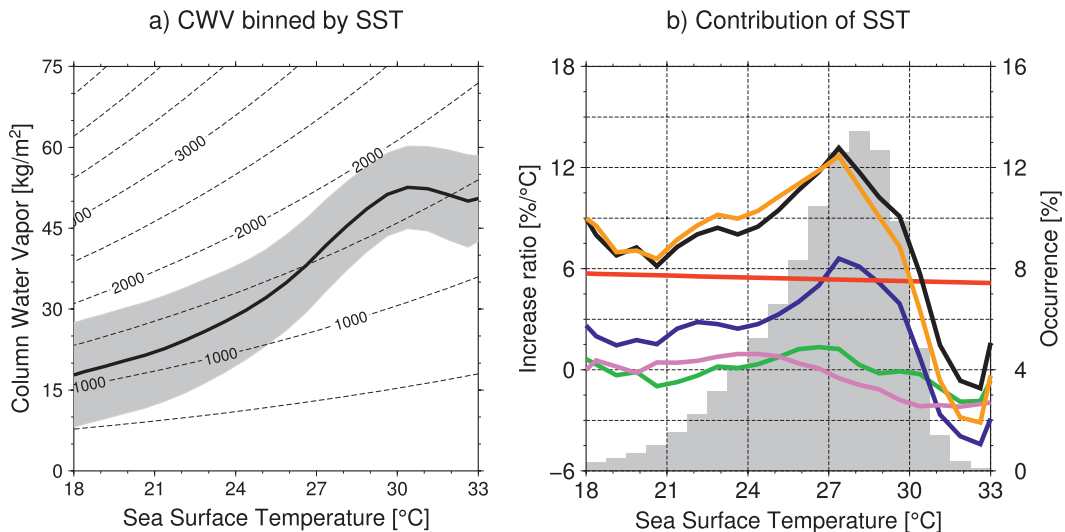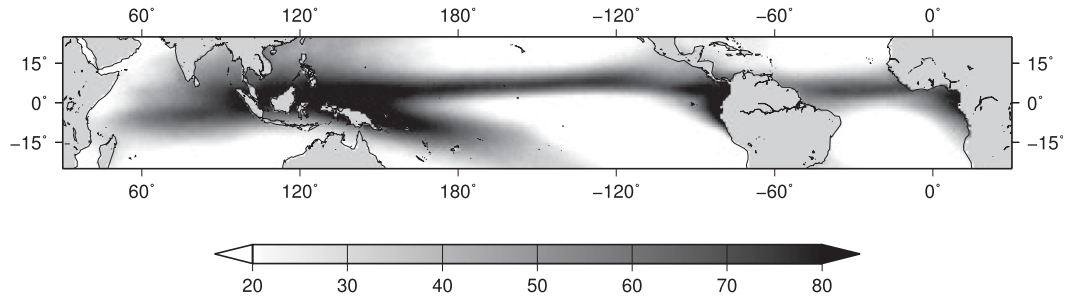## a) CWV binned by SST

b) Contribution of SST

FIG. 5. (a) As in Fig. 2a, but for CWV binned by SST (thick line). Standard deviation of ± 1 around mean CWV is shaded. Bin size is 0.75°C. (b) Observed estimates of each term in (6): $\partial \ln W / \partial T_s$ (orange), $\partial \ln RH_0 / \partial T_s$ (green), $\partial \ln H_v / \partial T_s$ (blue), the C–C relation (red), the sum of decomposed terms (black), and the residual term (violet). Shaded histogram shows SST occurrence (%).

FIG. 6. Occurrence (%) of the threshold H_v over 2200 m.

right-hand side in the bottom line of (6) are the sensitivity of RH_0 and H_v to SST, respectively. The third term represents the C–C relation. One can readily find that $R_v T_s$ is an order of magnitude smaller than L_v, so that the last term is virtually determined by the C–C relation. Figure 5b shows the contribution of each term in (6). The sum of the decomposed terms in (6) almost agrees with the actual sensitivity of CWV to SST, which justifies the utility of (6). The contribution of the third term is almost constant at about 6% °C^{-1} as predicted by the C–C relation. The C–C relation dominates the other two terms when SSTs are below 27°C; that is, the behavior of CWV is dominated primarily by the C–C relation with SST. On the other hand, the contribution of H_v is greatest from 27° to 29°C, implying that the increase of

H_v with SST is critical for the dependence of CWV on SST. The contribution of RH_0 to SST remains minimal as expected. The residual sensitivity to SST, defined as the difference between the CWV sensitivity and the sum of decomposed terms, arises from the difference between T_s and T_0 that has been neglected in (6).

Figure 6 shows the frequency of occurrence when H_v exceeds 2200 m on the global map. The threshold of 2200 m separates the two SST regimes as seen from Fig. 3b as discussed in the next section. Regions where H_v is higher than this threshold include the Indian Ocean, the tropical western Pacific, the intertropical convergence zone (ITCZ), and the South Pacific convergence zone (SPCZ). On the other hand, regions where H_v is generally below the threshold distribute over subtropical
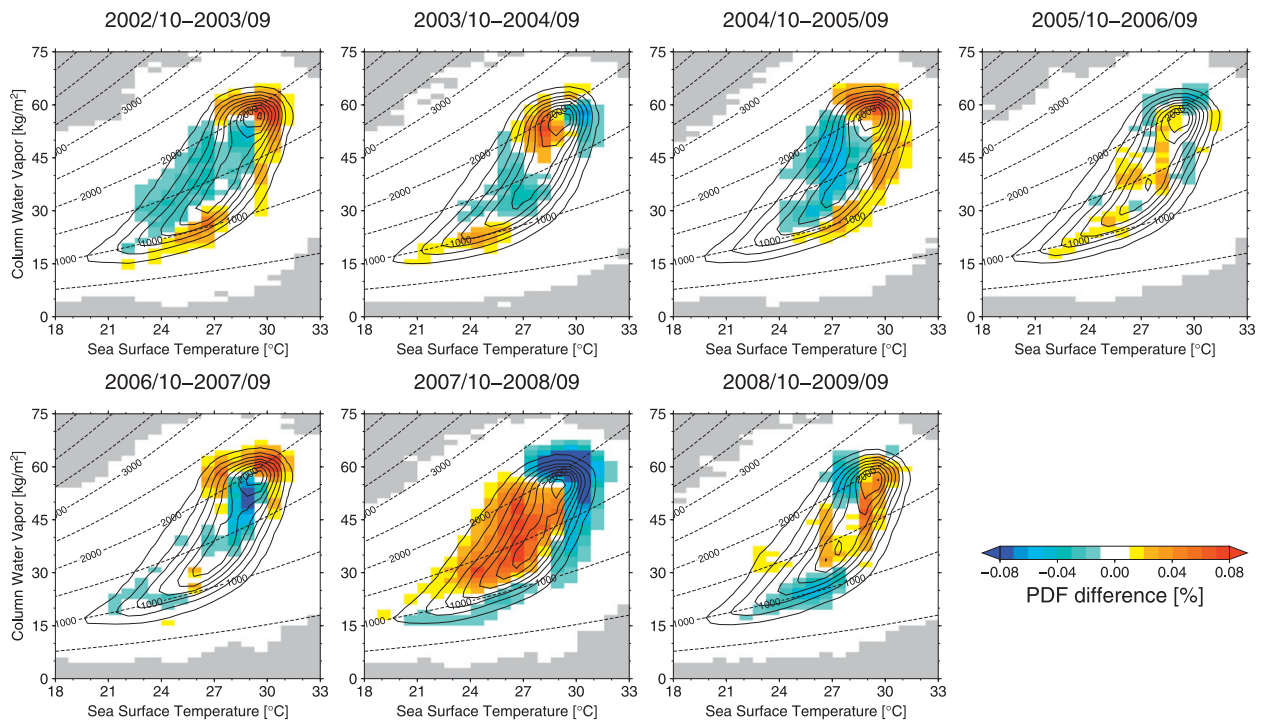

FIG. 7. As in Fig. 2a, but for the joint probability density function (PDF) separated for 7 years as indicated at the top of each panel. Color illustrates the anomaly against the 7-yr mean (Fig. 2).
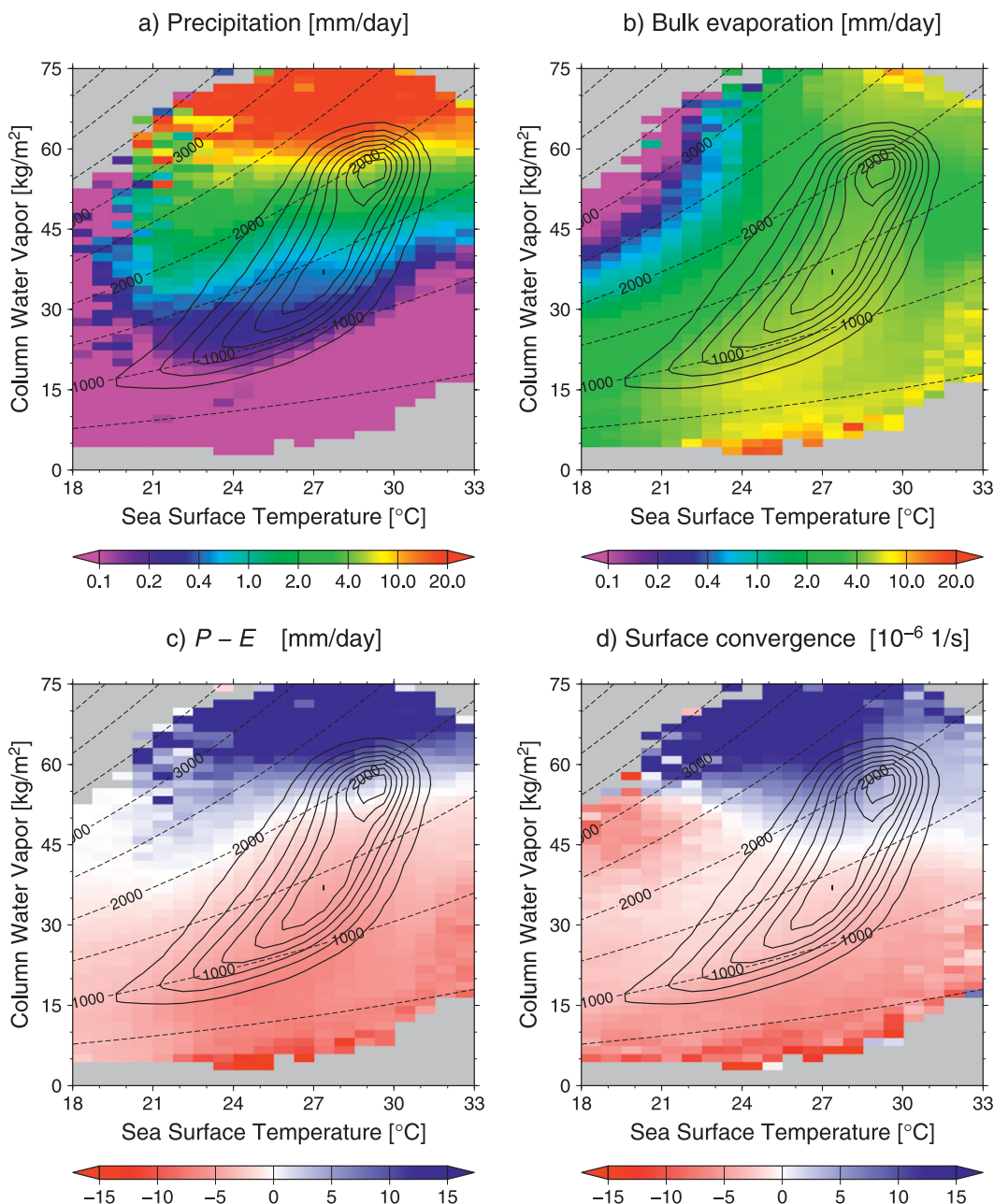
FIG. 8. As in Fig. 2a, but overlaid with (a) precipitation P (mm day^{-1}), (b) evaporation E (mm day^{-1}), (c) $P - E$ (mm day^{-1}), and (d) surface convergence (10^{-6} s^{-1}).

oceans surrounding tropical oceans. The two SST regimes are thus hereafter called subtropics and deep tropic regimes: H_v hardly changes in the subtropic regime and H_v increases with SST in the deep tropics regime.

The temporal variability of CWV is closely related with SST on a monthly time scale (Wentz and Schabel 2000; Trenberth et al. 2005). Trenberth et al. (2005) and Sudradjat et al. (2005) pointed out that the temporal variability of CWV relates with the El Niño–Southern

Oscillation (ENSO) variability. Figure 7 shows yearly histograms for the consecutive 12 months from October to September. Histograms are overall similar, but some systematic deviation is visible relative to the mean histogram for all 7 years combined. El Niño events are observed in 2002/03 and 2004/05 and a La Niña event is observed in 2007/08, and both El Niño and La Niña events occurred during 2006/07 according to the oceanic Niño index. The joint histograms between El Niño

a) Stdv. of P [mm/day]

b) Stdv. of E [mm/day]

c) Stdv. of $P - E$ [mm/day]
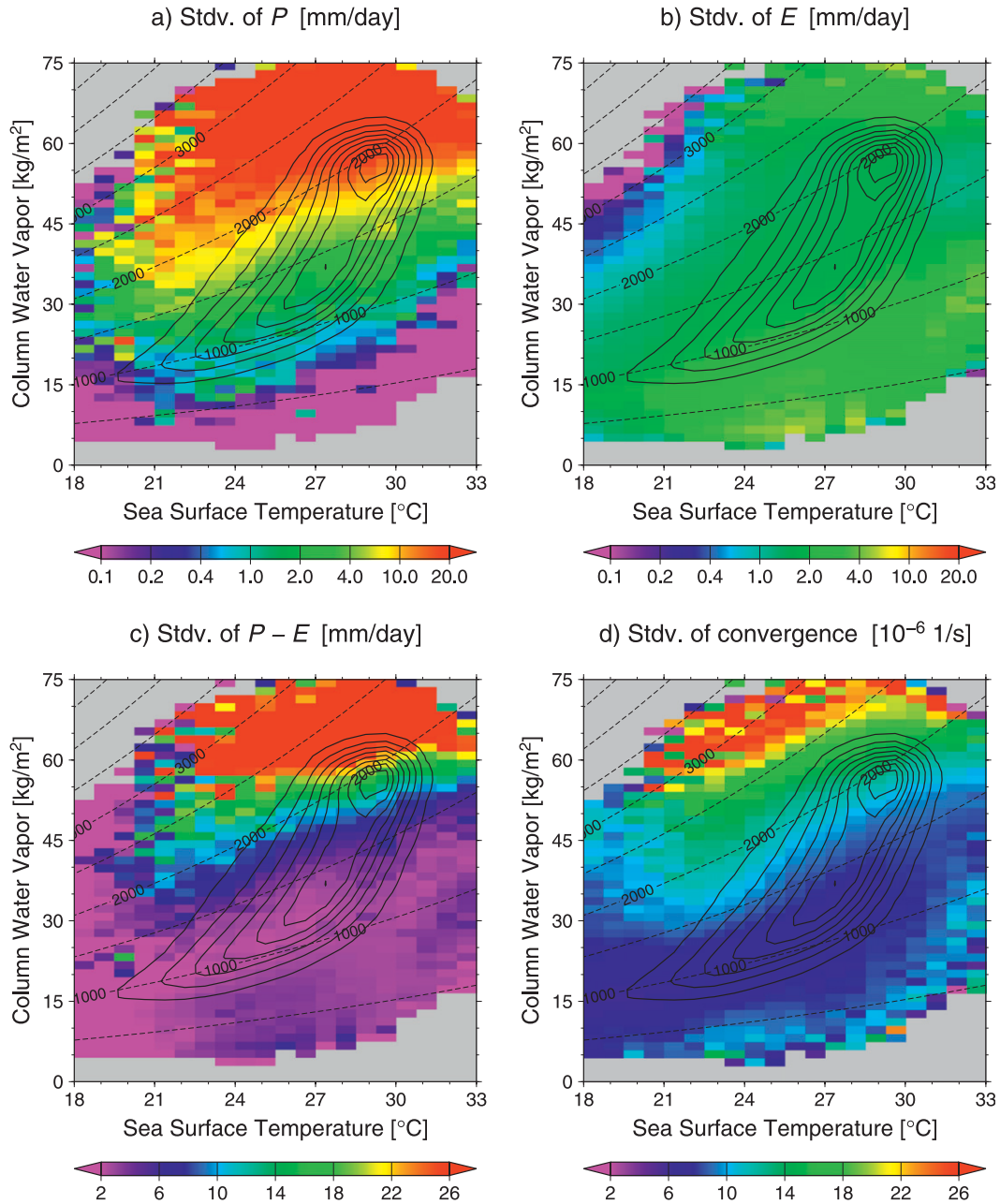
d) Stdv. of convergence [10^{-6} 1/s]

FIG. 9. As in Fig. 8, but for standard deviation.

and La Niña years are in contrast with each other. The occurrence in El Niño (La Niña) years enhances (reduces) at the top end of the histogram ridge and increases (decreases) along its lower tail. These ENSO-related changes are as expected given that the tropics as a whole has a warmer SST and a more humid atmosphere during El Niño. This variability, however, is not so large that it essentially alters the climatological histogram.

5. Discussion

In this section, contrasting behaviors of H_v between the subtropics and deep tropics regimes seen in the previous section are discussed. Figure 8 illustrates the parameters critical for the moisture budget in the SST–CWV plane. Figure 8a shows that precipitation P depends strongly on CWV rather than SST. The importance of water vapor for convective development was emphasized
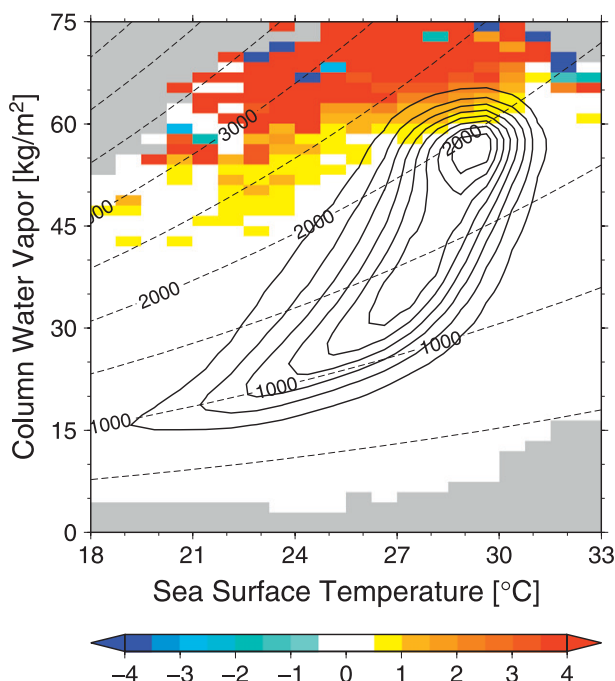
FIG. 10. The difference in P (mm day^{-1}) conditioned or unconditioned (unconditioned − conditioned) on AIRS and QuikSCAT data losses in heavily raining areas.

by Inoue (1990) and Neelin et al. (2009) while the strength of convection is also known to relate with SST (Gadgil et al. 1984; Graham and Barnett 1987) presumably through the tight correlation between SST and CWV. The sharp dependence of P on CWV is consistent with the known exponential relationship between CWV and P (Zeng 1999; Bretherton et al. 2004; Peters and Neelin 2006). The influence of SST, however, appears to be indirect because P remains relatively weak even for the highest SSTs as far as CWV is low. Evaporation E (Fig. 8b) is relatively homogeneous across the entire domain when plotted in logarithmic scale, in sharp contrast to P, which changes drastically in the same color scale (Fig. 8a). The difference between the two, $P - E$, is thus virtually a mirror image of P, decreasing from positive to negative across their boundary around a CWV of 50 kg m^{-2} (Fig. 8c). An excess and deficit of $P - E$ is nearly balanced with moisture convergence and divergence (Peixoto and Oort 1992), as seen in Fig. 8d although only the surface divergence is plotted instead of moisture divergence. Figure 8d shows that the surface convergence crosses zero at about a CWV of 45 kg m^{-2}, similarly to $P - E$ (Fig. 8c). Figure 9 shows the standard deviation for Fig. 8. The standard deviation of P (Fig. 9a) varies sharply depending on both SST and CWV while the variation of E (Fig. 9b) is rather homogeneous. Consequently, the standard deviation of $P - E$ (Fig. 9c) mainly reflects that
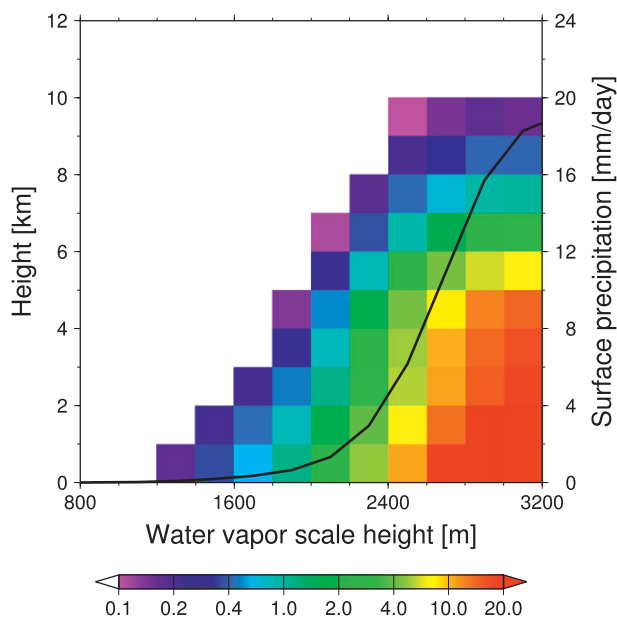
of P, which is roughly mirrored by the standard deviation of surface convergence (Fig. 9d). The standard deviation stays small along the histogram ridge, so the relation between CWV and SST may be considered to be overall stable around the climatology. The large variability of P is observed where P itself is high, and might be partly linked with a significant reduction of sample size because of rain contamination in AMSR-E, AIRS, and

FIG. 11. As in Fig. 1, but for vertical precipitation structure (mm day^{-1}). The solid line shows surface precipitation (mm day^{-1}) binned by the water vapor scale height.
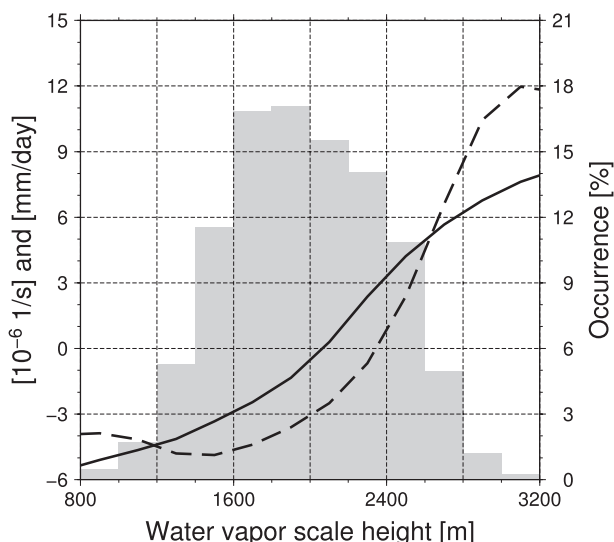

FIG. 12. Surface convergence (solid) (10^{-6} s^{-1}) and $P - E$ (dashed) (mm day^{-1}) sorted by the water vapor scale height. Shaded histogram shows H_v occurrence (%).

TABLE 1. Frequency-of-occurrence chart of H_v and $P - E$ with given thresholds ($H_v = 2200$ m and $P - E = 0$ mm day^{-1}). The classification is performed with the local climatology of H_v and $P - E$. Numbers show the count of $1° \times 1°$ grid boxes over the ocean in the analysis area.

		$P - E$ (mm day^{-1})		
		>0	<0	Total
	>2200	2218	666	2884
H_v (m)	<2200	226	10 027	10 253
	Total	2444	10 693	13 137

QuikSCAT observations. Figure 10 shows the difference in P conditioned or unconditioned on AIRS and QuikSCAT data losses in heavily raining areas. Figure 10 virtually illustrates the sampling bias owing to precipitation in water vapor and surface wind estimates. A systematic bias is found where P is very high, but the significantly biased domain does not extend down to the histogram ridge and its close vicinity. Rainfall biases do exist but would not alter the main conclusions of this paper as far as global-scale climatology is concerned. AMSR-E SST (used for the abscissa) may be also affected by rain, but this effect is minor since Fig. 10 remains almost unchanged when the National Oceanic and Atmospheric Administration (NOAA) Optimum Interpolation SST (OISST; Reynolds et al. 2002) is used for plotting the same diagram instead of AMSR-E SST (not shown).

Figure 11 shows the vertical precipitation structure separately for different H_v. An increase of H_v accompanies a rapid deepening of convection and an increase

of P. The systematic change in H_v related with P corresponds well to FT moisture variation in Fig. 1, which is consistent with past observational studies (Bretherton et al. 2004; Holloway and Neelin 2009). Figure 12 shows the moisture budget parameters as a function of H_v. Surface convergence and $P - E$ intersect the zero when H_v is 2100 and 2400 m, respectively. The threshold of H_v in the moisture budget can be therefore considered to be about 2200 m, which separates the subtropics regime and the deep tropics regime as already seen in Fig. 6. To ensure this possible link between H_v and climate regimes, Table 1 shows a frequency occurrence chart of H_v and the sign of $P - E$ computed from the global climatology map. Areas with $H_v > 2200$ m generally have more precipitation than evaporation and vice versa, with some exceptions with relatively less frequencies of occurrence. This result overall supports the regime classification based on the H_v threshold of 2200 m. It is near the boundary between the deep tropics and subtropics (Fig. 6) that the classification fails.

Based on the present results and discussions above, the regional difference in the SST–CWV relation along the histogram ridge between subtropical and tropical oceans can be schematically illustrated in Fig. 13. In the subtropics regime, surface divergence removes the BL moisture supplied by surface evaporation while vertical moisture transport from the BL to the FT is suppressed in the absence of vigorous convection. The inefficient vertical moisture transport holds moisture close to the surface, resulting in a consistently low value of H_v. On the other hand, in the deep tropics regime where deep convection dominates, convection effectively ventilates
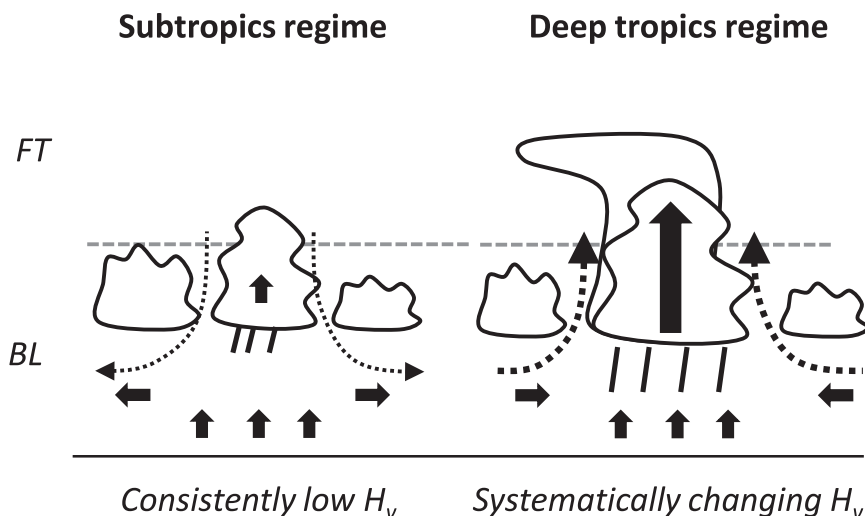

FIG. 13. The schematics of the moisture budget characteristics in the subtropics and deep tropics regimes. Solid arrows show the moisture flux. Dashed lines with arrows show surface divergence and convergence.
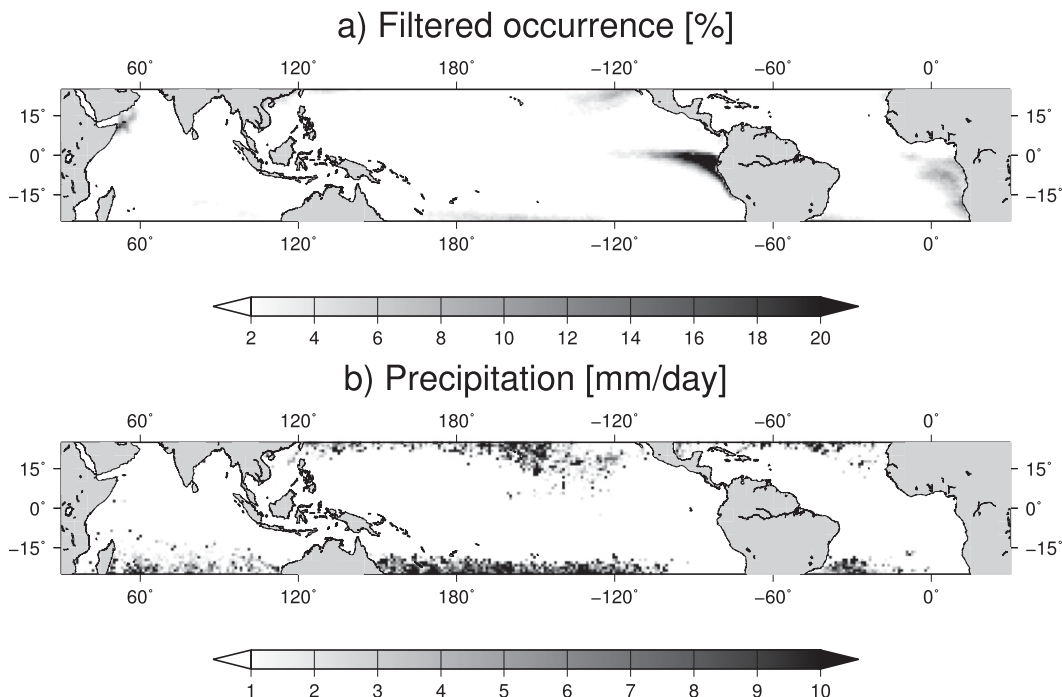
a) Filtered occurrence [%]

b) Precipitation [mm/day]

FIG. 14. (a) Frequency of occurrence (%) for SSTs from 18° to 24°C and CWVs from 40 to 55 kg m^{-2}. (b) Precipitation (mm day^{-1}) conditioned on the same SST and CWV ranges.

the BL against surface moisture convergence, which leads to an efficient FT moistening. As a result, H_v increases as convection intensifies unlike in the subtropics regime. Both the deep tropics and subtropics regimes result in the balance of surface moisture although individual processes are quite different from each other.

Stephens (1990) found that the CWV variability is controlled by SST in a way resembling the C–C relation over global oceans, while the relationship is somewhat loosened over tropical oceans (Gaffen et al. 1992; Jackson and Stephens 1995). In light of the present study, the conclusion of Stephens (1990) applies to the subtropics but does not to the deep tropics, where H_v changes systematically with SST and CWV no longer behaves as expected from the C–C relation. On the other hand, Holloway and Neelin (2009) showed that the CWV variability observed in situ sounding in the western Pacific is explained mainly by the FT moisture rather than coupled closely to SST. This is consistent with our findings for the deep tropics regime. It was also pointed out by other work (e.g., Bretherton et al. 2004) that precipitation nonlinearly increases with the FT moisture. This steep increase of precipitation signifies the characteristics typical of the deep tropics, although not always specifically intended so in past work. As such, the present conclusions provide a comprehensive picture covering both the deep tropics and subtropics that have been individually examined by difference studies.

In some domains in the SST–CWV diagram, $P - E$ and surface convergence have opposite signs, implying that the balance as shown in Fig. 13 does not hold. To identify the origins of such an imbalance, the domain of SSTs from 18° to 24°C and CWVs from 40 to 55 kg m^{-2} is projected back onto a global map (Fig. 14). Figure 14a shows that the selected SSTs and CWVs are found over the cold tongue in the south of the ITCZ where P is generally low. A substantial amount of precipitation that falls in these SST and CWV ranges is attributed to extratropical storms (Fig. 14b) although observed occurrence is extremely infrequent. The apparent budget imbalance in this case thus likely arises because statistically rare high-precipitation events in midlatitudes contaminate the cold tongue climatology when sorted by SST and CWV. In addition, cold tongue regions may be exposed to occasional intrusions of ITCZ disturbances, which could make it difficult to characterize these regions in terms of the simple two-regime classifications as shown in Fig. 13.

6. Summary

In the current study, the regional difference in the relationship between SST and CWV is evaluated over tropical and subtropical oceans with a focus on the potential roles of vertical moisture gradient. Satellite data acquired by the *Aqua* AMSR-E and AIRS/AMSU suite,

the QuikSCAT SeaWinds, and the TRMM PR are analyzed together for 7 years from October 2002 to September 2009 over the latitudinal band between 25°N and 25°S.

This study focuses on the water vapor scale height H_v as an index of vertical moisture gradient between the boundary layer and the free troposphere. It is found that the SST–CWV relation changes its nature depending on the range of SST. The SST–CWV relation resembles the C–C relation when SST is lower than 27°C. For higher SSTs, the SST–CWV relation does not follow the C–C relation because the sensitivity of CWV to H_v is larger than the SST contribution, although surface relative humidity remains constant. When mapped globally, H_v hardly changes over relatively cold ocean in the subtropics and increases with SST in the deep tropics where SST is high. The subtropics and deep tropics regimes clearly separate two climate regimes with distinct behaviors of H_v as noted above. The interannual variability of the SST–CWV relation related with the El Niño–Southern Oscillation variability is found that the histograms of SST and CWV is slightly changed from year to year while the overall pattern is almost unchanged.

The different behaviors of H_v between the regimes are discussed in terms of the regional moisture budget including vertical moisture transport through convection. In the subtropics regime, surface divergence removes the boundary layer moisture supplied by surface evaporation while moisture transport from the boundary layer to the free troposphere is suppressed in the absence of vigorous convection because of the subsidence branch of the Hadley and Walker circulation. The inefficient vertical moisture transport holds moisture close to the surface, which results in a consistently low H_v. On the other hand, in the deep tropics regime where deep convection dominates, convection effectively ventilates the boundary layer moisture against surface moisture convergence, which leads to an efficient free troposphere moistening. As a result, H_v increases as convection intensifies unlike in the subtropics regime. This two-regime picture does break down in some regions including the east Pacific cold tongue. The temporal variation of moisture between the boundary layer and the free troposphere will be explored in future work.

APPENDIX A

Estimation of Surface Moisture and Evaporation

In this study, surface water vapor mixing ratio $q_{v,s}$ is estimated by a simple BL model including a surface layer (SL) (Fig. A1) to obtain the water vapor scale height and evaporation. The BL model is based on cloud-topped BL within the SL characterized by the logarithmic law. The BL model is originally formulated by Masunaga (2012) for estimating water vapor mixing ratio below the mixed layer (ML) or $q_{v,\mathrm{ML}}$. When the SL is neutrally stable, the vertical gradient of moisture is expressed as a logarithmic profile, that is,

$$q_{v,s} = q_{v,\mathrm{ML}} + \frac{\ln(z/z_{\mathrm{SL}})}{\ln(z_q/z_{\mathrm{SL}})}[q_v^*(T_s) - q_{v,\mathrm{ML}}], \quad \text{(A1)}$$

$q_v^*(T_s)$, z, z_{SL}, and z_q are saturation vapor mixing ratio for sea surface temperature T_s, the height, the SL height, and the roughness length for moisture, respectively. The theoretical bulk transfer coefficients for momentum C_D and for evaporation C_E are (Garratt 1992)

$$C_D(z) = \left[\frac{\kappa}{\ln(z/z_0)}\right]^2 \quad \text{and} \quad \text{(A2)}$$

$$C_E(z) = \frac{\kappa}{\ln(z/z_0)}\frac{\kappa}{\ln(z/z_q)}, \quad \text{(A3)}$$

where κ and z_0 are von Kármán constant (=0.40) and the surface roughness length corresponding to the height of zero wind speed, respectively. From (A2) and (A3), the relationship between C_D and C_E becomes

$$C_E(z) = \frac{\kappa}{\ln(z/z_q)}\sqrt{C_D(z)}. \quad \text{(A4)}$$

Large et al. (1994) gives the empirical relationship at 10-m height between C_D and C_E as
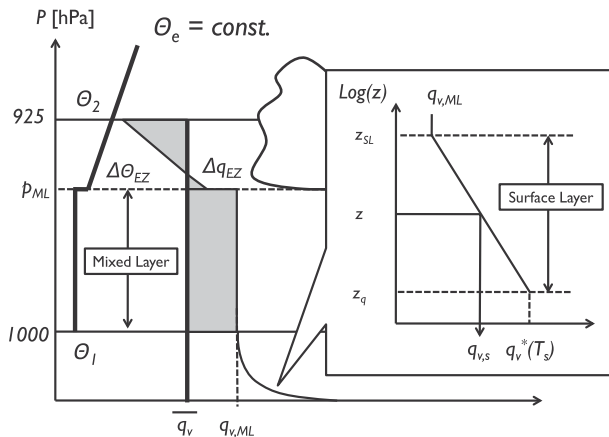
FIG. A1. (left) The schematics of the BL and SL model to estimate surface water vapor mixing ratio $q_{v,s}$. The BL model estimating mixed layer water vapor mixing ratio $q_{v,ML}$ is taken from by Masunaga (2012). (right) The estimation of $q_{v,ML}$ in the SL model is logarithmically extrapolated down to $q_{v,s}$ and saturated water vapor mixing ratio $q_v^*(T_s)$ for sea surface temperature T_s.

$$C_E(10) = \frac{34.6}{10^3} \sqrt{C_D(10)}. \tag{A5}$$

Therefore, z_q is calculated from (A4) and (A5),

$$z_q = 10 \exp\left(-\frac{10^3}{34.6}\kappa\right), \tag{A6}$$

where z_q is obtained as 9.534×10^{-5} m and fixed in the current SL model. In this study, z_{SL} is assumed to be 50 m. Figure A2 shows the result of comparison between satellite estimated $q_{v,s}$ and the in situ $q_{v,s}$. The in situ $q_{v,s}$ is obtained by the Tropical Atmosphere Ocean (TAO) arrayed buoys over tropical oceans. Satellite overpasses and buoy locations are matched up within 1° resolution. The observed height of $q_{v,s}$ in the TAO buoys is 3-m height, so that $q_{v,s}$ is calculated in (A1) as 3 m. Figure A2a is the joint probability density function between in situ $q_{v,s}$ and AIRS lowest q_v, which corresponds to layer mean between 1000 and 925 hPa. While AIRS lowest q_v is clearly underestimated, the estimation of $q_{v,s}$ from the BL model by (A1) reasonably agrees with the in situ measurements in the current method (Fig. A2b).

Finally, evaporation E is calculated from the bulk method,

$$E = \rho_a C_E |\mathbf{u}_{10}|[q_v^*(T_s) - q_{v,s}], \tag{A7}$$

where ρ_a and $|\mathbf{u}_{10}|$ are the density of dry air ($=1.2$ kg m^{-3}) and the wind speed at 10 m, respectively. Here, C_E is adopted from the empirical formulas derived by Large et al. (1994),

$$C_D = \frac{1}{10^3}\left(\frac{2.70}{|\mathbf{u}_{10}|} + 0.142 + 0.0764|\mathbf{u}_{10}|\right), \tag{A8}$$

and (A5). In this study, $|\mathbf{u}_{10}|$ is obtained by QuikSCAT.

(a) AIRS 1000–925 hPa mean q_v (b) AIRS/AMSR–E estimated $q_{v,s}$
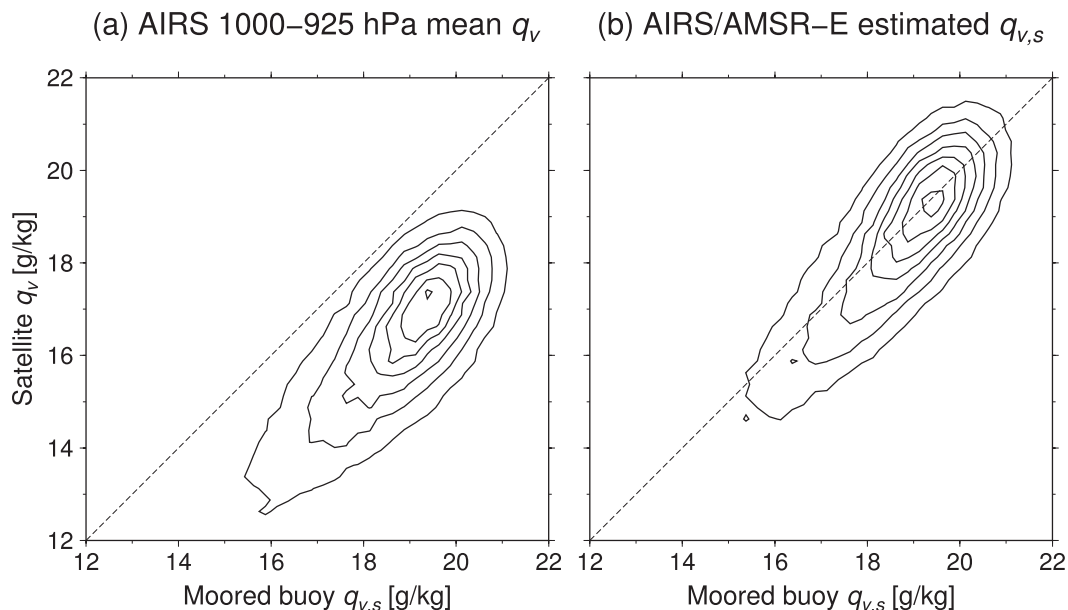

FIG. A2. (a) The joint probability density function between $q_{v,s}$ observed by TAO buoy and AIRS layer-mean q_v between 1000 and 925 hPa. Bin sizes are both 0.25 g kg^{-1}. Contour interval is 0.1%. (b) As in (a), but for $q_{v,s}$ estimated by AMSR-E and AIRS.

TABLE B1. Error analysis for each observed parameter. Bias, RMSE, and correlation coefficient r are calculated against in situ data. "Intp" indicates whether or not interpolation is applied. Precipitation P is computed with TRMM PR each for sample.

	Intp	No.	Bias	RMSE	r	P (mm day^{-1})
All samples	—	53 716	—	—	—	3.65
T_s (°C)	no	51 136	−0.03	0.51	0.97	2.93
	yes	53 603	−0.03	0.51	0.97	3.59
T_0 (°C)	no	47 206	−1.43	1.68	0.77	2.47
	yes	52 591	−1.14	1.73	0.76	3.32
$q_{v,s}$ (g kg^{-1})	no	46 431	−0.21	1.16	0.82	2.34
	yes	52 568	−0.20	1.16	0.82	3.32
$|\mathbf{u}_{10}|$ (m s^{-1})	no	52 366	0.16	1.22	0.86	3.20
	yes	53 706	0.18	1.24	0.86	3.64
u_{10} (m s^{-1})	no	53 366	0.00	1.59	0.91	3.20
	yes	53 706	−0.02	1.62	0.90	3.64
v_{10} (m s^{-1})	no	53 366	0.20	1.59	0.91	3.20
	yes	53 706	0.20	1.59	0.90	3.64
E (mm day^{-1})	no	45 688	0.20	1.26	0.75	2.34
	yes	52 560	0.24	1.32	0.73	3.32

APPENDIX B

Error Estimation of Interpolated Data

The accuracy of satellite estimations by AMSR-E, AIRS, and QuikSCAT is affected by rain and/or clouds. In this study, data gaps caused by rain and clouds are spatially interpolated from surrounding areas to reduce sampling bias that could lead to an underestimation of precipitation. The interpolation is done by averaging together the neighboring eight grid boxes. The impact of the interpolation is evaluated in comparison with in situ data obtained by the TAO arrayed buoys. Methodology is as described in appendix A, but data are sampled only when AMSR-E, AIRS, QuikSCAT, and PR observations and in situ data are not subject to this limitation. QuikSCAT measures wind speed at 10-m height, while the TAO anemometers observe wind speed at 4-m height. The wind speed measured by the TAO buoys is converted to the equivalent neutral wind speed at the 10-m height by the method of Liu and Tang (1996). Table B1 shows bias, root-mean-square error (RMSE), correlation coefficient r, and PR precipitation P computed for each sample composed of satellite estimations and in situ observations. Parameters assessed are sea surface temperature T_s, surface air temperature T_0, surface water vapor mixing ratio $q_{v,s}$, scalar wind speed at 10-m height $|\mathbf{u}_{10}|$, zonal wind u_{10}, meridional wind v_{10}, and evaporation E. Estimates with and without interpolation are compared for each parameter. Estimated $q_{v,s}$ and E rely on AIRS and 10%–15% of samples are lost without interpolation, while the loss of data is a few percent for AMSR-E T_s and QuikSCAT wind speed. Interpolated data tend to be somewhat lower in accuracy than non-interpolated data but do not introduce a significant sampling bias in precipitation. Precipitation can be substantially underestimated because of the sampling bias when the interpolations are not applied. The accuracy of estimated $q_{v,s}$ is 1.2 g kg^{-1}, which is same or better than the typical accuracy of satellite product in the range from 1.2 to 2.0 g kg^{-1} (Iwasaki and Kubota 2012). Bourras (2006) showed that the accuracy of E from existing satellite products against tested in situ data over tropical oceans is from 24 to 41 W m^{-2}, which corresponds to a range from 0.8 to 1.4 mm day^{-1}. RMSE of the current estimation of E is 1.3 mm day^{-1}.

REFERENCES

Bolsenga, S., 1965: The relationship between total atmospheric water vapor and surface dew point on a mean daily and hourly basis. *J. Appl. Meteor.,* **4,** 430–432.

Bolton, D., 1980: The computation of equivalent potential temperature. *Mon. Wea. Rev.,* **108,** 1046–1053.

Bourras, D., 2006: Comparison of five satellite-derived latent heat flux products to moored buoy data. *J. Climate,* **19,** 6291–6313.

Bretherton, C., M. Peters, and L. Back, 2004: Relationships between water vapor path and precipitation over the tropical oceans. *J. Climate,* **17,** 1517–1528.

Chaboureau, J.-P., A. Chédin, and N. A. Scott, 1998: Relationship between sea surface temperature, vertical dynamics, and the vertical distribution of atmospheric water vapor inferred from TOVS observations. *J. Geophys. Res.,* **103** (D18), 23 173–23 180.

Dai, A., 2006: Recent climatology, variability, and trends in global surface humidity. *J. Climate,* **19,** 3589–3606.

Ebuchi, N., H. C. Graber, and M. J. Caruso, 2002: Evaluation of wind vectors observed by QuikSCAT/SeaWinds using ocean buoy data. *J. Atmos. Oceanic Technol.,* **19,** 2049–2062.

Fetzer, E., B. Lambrigtsen, A. Eldering, H. Aumann, and M. Chahine, 2006: Biases in total precipitable water vapor climatologies from Atmospheric Infrared Sounder and Advanced Microwave Scanning Radiometer. *J. Geophys. Res.,* **111,** D09S16, doi:10.1029/2005JD006598.

Gadgil, S., N. Joshi, and P. Joseph, 1984: Ocean–atmosphere coupling over monsoon regions. *Nature,* **312,** 141–143.

Gaffen, D., W. Elliott, and A. Robock, 1992: Relationships between tropospheric water vapor and surface temperature as observed by radiosondes. *Geophys. Res. Lett.,* **19,** 1839–1842.

Garratt, J., 1992: *The Atmospheric Boundary Layer.* Cambridge University Press, 316 pp.

Graham, N., and T. Barnett, 1987: Sea surface temperature, surface wind divergence, and convection over tropical oceans. *Science,* **238,** 657–659.

Holloway, C., and J. Neelin, 2009: Moisture vertical structure, column water vapor, and tropical deep convection. *J. Atmos. Sci.,* **66,** 1665–1683.

Iguchi, T., T. Kozu, R. Meneghini, J. Awaka, and K. Okamoto, 2000: Rain-profiling algorithm for the TRMM precipitation radar. *J. Appl. Meteor.,* **39,** 2038–2052.

Inoue, T., 1990: The relationship of sea surface temperature and water vapor amount to convection over the western tropical Pacific revealed from split window measurements. *J. Meteor. Soc. Japan,* **68,** 590–606.

Iwasaki, S., and M. Kubota, 2012: Algorithms for estimation of air-specific humidity using TMI data. *Int. J. Remote Sens.,* **33,** 7413–7430.

Jackson, D., and G. Stephens, 1995: A study of SSM/I-derived columnar water vapor over the global oceans. *J. Climate,* **8,** 2025–2038.

Large, W., J. McWilliams, and S. Doney, 1994: Oceanic vertical mixing: A review and a model with a nonlocal boundary layer parameterization. *Rev. Geophys.,* **32,** 363–403.

Liu, W. T., and P. Niiler, 1984: Determination of monthly mean humidity in the atmospheric surface layer over oceans from satellite data. *J. Phys. Oceanogr.,* **14,** 1451–1457.

——, and W. Tang, 1996: Equivalent neutral wind. JPL Publ. 96-17, 16 pp. [Available online at http://airsea-www.jpl.nasa.gov/data/data.html.]

Masunaga, H., 2012: A satellite study of the atmospheric forcing and response to moist convection over tropical and subtropical oceans. *J. Atmos. Sci.,* **69,** 150–167.

Neelin, J. D., O. Peters, and K. Hales, 2009: The transition to strong convection. *J. Atmos. Sci.,* **66,** 2367–2384.

Peixoto, J. P., and A. H. Oort, 1992: *Physics of Climate.* American Institute of Physics, 520 pp.

——, and ——, 1996: The climatology of relative humidity in the atmosphere. *J. Climate,* **9,** 3443–3463.

Peters, O., and J. Neelin, 2006: Critical phenomena in atmospheric precipitation. *Nat. Phys.,* **2,** 393–396.

Prabhakara, C., G. Dalu, R. C. Lo, and N. R. Nath, 1979: Remote sensing of seasonal distribution of precipitable water vapor over the oceans and the inference of boundary layer structure. *Mon. Wea. Rev.,* **107,** 1388–1401.

Raval, A., and V. Ramanathan, 1989: Observational determination of the greenhouse effect. *Nature,* **342,** 758–761.

Reitan, C., 1963: Surface dew point and water vapor aloft. *J. Appl. Meteor.,* **2,** 776–779.

Reynolds, R. W., N. A. Rayner, T. M. Smith, D. C. Stokes, and W. Wang, 2002: An Improved in situ and satellite SST analysis for climate. *J. Climate,* **15,** 1609–1625.

Smith, W., 1966: Note on the relationship between total precipitable water and surface dew point. *J. Appl. Meteor.,* **5,** 726–727.

Stephens, G., 1990: On the relationship between water vapor over the oceans and sea surface temperature. *J. Climate,* **3,** 634–645.

Sudradjat, A., R. R. Ferraro, and M. Fiorino, 2005: A comparison of total precipitable water between reanalyses and NVAP. *J. Climate,* **18,** 1790–1807.

Susskind, J., C. Barnet, and J. Blaisdell, 2003: Retrieval of atmospheric and surface parameters from AIRS/AMSU/HSB data in the presence of clouds. *IEEE Trans. Geosci. Remote Sens.,* **41,** 390–409.

——, J. Blaisdell, L. Iredell, and F. Keita, 2011: Improved temperature sounding and quality control methodology using AIRS/AMSU Data: The AIRS science team version 5 retrieval algorithm. *IEEE Trans. Geosci. Remote Sens.,* **49,** 883–907.

Tobin, D. C., and Coauthors, 2006: Atmospheric Radiation Measurement site atmospheric state best estimates for Atmospheric Infrared Sounder temperature and water vapor retrieval validation. *J. Geophys. Res.,* **111,** D09S14, doi:10.1029/2005JD006103.

Trenberth, K., J. Fasullo, and L. Smith, 2005: Trends and variability in column-integrated atmospheric water vapor. *Climate Dyn.,* **24,** 741–758.

Wentz, F. J., and T. Meissner, 2000: AMSR ocean algorithm, version 2. Remote Sensing Systems Rep. No. 121599A-1, 66 pp. [Available online at http://www.ssmi.com/papers/amsr/AMSR_Ocean_Algorithm_Version_2.pdf.]

——, and M. Schabel, 2000: Precise climate monitoring using complementary satellite data sets. *Nature,* **403,** 414–416.

Zeng, X., 1999: The relationship among precipitation, cloud-top temperature, and precipitable water over the tropics. *J. Climate,* **12,** 2503–2514.

Zhang, C., and F. Qiu, 2008: Empirical relationship between sea surface temperature and water vapor: Improvement of the physical model with remote sensing derived data. *J. Oceanogr.,* **64,** 163–170.